POLITECNICO DI TORINO
Repository ISTITUZIONALE

Performance Analysis of a Noncontact Plastic Fiber Optical Fiber Displacement Sensor with Compensation of Target Reflectivity

(Article begins on next page)

24 April 2024

Research Article

Performance Analysis of a Noncontact Plastic Fiber Optical Fiber Displacement Sensor with Compensation of Target Reflectivity

Daniele Tosi,[1] Guido Perrone,[2] and Alberto Vallan[2]

[1] *Optical Fibre Sensors Research Centre, Department of Electronic and Computer Engineering, University of Limerick, Limerick, Ireland*
[2] *Department Electronics and Telecommunications, Politecnico di Torino, Corso Duca degli Abruzzi 24, 10129 Torino, Italy*

Correspondence should be addressed to Guido Perrone; guido.perrone@polito.it

An inexpensive fiber-based noncontact distance sensor specific for monitoring short-range displacements in micromachining applications is presented. To keep the overall costs low, the sensor uses plastic optical fibers and an intensiometric approach based on the received light intensity after the reflection from the target whose displacement has to be measured. A suitable target reflectivity compensation technique is implemented to mitigate the effects due to target surface nonuniformity or ageing. The performances of the sensor are first evaluated for different fiber configurations and target reflectivity profiles and positions using a numerical method based on Monte Carlo simulations. Then, experimental validations on a configuration designed to work up to 1.5 mm have been conducted. The results have confirmed the validity of the proposed sensor architecture, which demonstrated excellent compensation capabilities, with errors below 0.04 mm in the (0-1) mm range regardless the color and misalignment of the target.

1. Introduction

Fiber Optic Sensors (FOSs) have gained an ever increasing attention in recent years due not only to the their excellent performances with respect their electromechanical counterparts, but also to the availability of high-quality off-the-shelf photonic components as side products of the enormous progress in optical communications.

FOSs are typically characterized by a high sensitivity joined with other unique characteristics such as lightweight, resistance to corrosion, immunity to electrostatic discharges, impossibility to start fires, and capability of remote operation using the same fiber both for sensing and for data transmission. However, despite the many sensing principles and implementations already proposed in the literature, their diffusion in everyday use is still confined to niche applications, mainly because of the high costs of the interrogators and of the complexity of optical layouts and interconnections.

Today, commercial FOSs are based on glass fibers similar to those used for high-performance optical communications, although Plastic Optical Fibers (POFs) are emerging as an alternative technology for the realization of inexpensive fiber

sensors and interconnections [1]. The "low cost" aspect is a crucial point to open up new market perspectives, since budget limitations often prevent permanent monitoring from being set up using fiber sensors even in cases where fibers are known to provide superior performances. Examples are in cultural heritage preservation (where, e.g., the intrinsic fire safety is a key requirement) or in industrial plant monitoring (where immunity from electromagnetic emissions and resistance to corrosion are requested).

POFs used in sensing are usually of the step index type, made by a poly-methyl-methacrylate (PMMA) large area core (from 0.25 mm to 0.98 mm diameter) surrounded by a thin fluoropolymer (some 10 micrometers). In all cases the numerical aperture (NA) is very high, being close to 0.5, and the combination of large core diameters and high NA accounts for the possibility of using inexpensive LED sources and the simplification in connectors and in sensor deployment, making plastic-fiber-based sensors an excellent competitor with respect to electromechanical sensors.

Although several sensing techniques have been described in the literature, POFs are best suited for intensiometric sensors, which are sensors that exploit the variation of the

received light intensity with the quantity under measurement. A simple intensiometric sensor for the measurement of distance can be arranged exploiting the variation of light collected between facing fibers [2]; the same principle can also be exploited in a noncontact setup if the receiving fiber collects the light from a moving target after a free space propagation span [3]. Despite its simplicity, this setup has already proved to be effective for monitoring vibrating targets [4], while this paper aims to analyze the design issues related to its use in measuring static displacements in short-range applications.

Measuring short distances without contact, indeed, is a very relevant problem in many areas of engineering, such as in precision micromechanics for monitoring small moving parts, and the optic-based approach is well suited for this application because it does not introduce perturbations, even in the case of submillimeter objects. Although several free space solutions have been proposed [5, 6], a fiber-based sensor provides further interesting features, such as an intrinsic simplification in positioning the sensing head in front of the moving object joined with the possibility to place the electronic control circuitry in a remote safe and electromagnetically quiet environment.

Intensiometric fiber-based implementations, however, have the main drawback of being very sensitive both to the geometric parameters of the sensing head (e.g., the angle at which the fiber tips are cut or the precise positioning of the fibers) and to the target reflectivity. The latter is the most problematic parameter. Indeed, while the geometric parameters are fixed and can be accounted for by a characterization of the sensor prior to its usage, the target reflectivity can change with time; examples of this variation in static conditions are day/night transitions, shadowing, yellowing due to aging, superficial dust, deposition of dirty spots, and so forth. Such change of reflectance conditions requires a proper compensation technique, so that it is possible to determine the displacement independently from target surface characteristics and reflectivity. In vibration measurements, it is possible to devise a compensation algorithm taking advantage of accelerometers already present in the vibration measurement setup [4], but this approach is not practicable for the determination of distance in static cases. The authors have already proposed a preliminary solution in [7], but a thorough investigation of a sensor setup able to make the displacement readout independent from the target reflectivity is still missing. This feature is essential to apply the sensor without precharacterizing the target surface and also to compensate variations of the target reflectance and of the launched power. In this paper, the effectiveness of the proposed measurement approach is first tested using Monte Carlo based numerical simulations and then through experiments.

The paper is organized as follows: Section 2 describes the architecture of the system and its working principle; Section 3 provides a numerical simulation of the optical system based on Monte Carlo and addresses the performance analysis; Section 4 reports some experimental results; finally, in Section 5, conclusions are drawn.

2. The Sensing System Setup

2.1. Basic Sensing Head Configuration. Simple, and thus low-cost, fiber optic noncontact distance sensors exploit the variation with distance of the light intensity reflected from the target, using a configuration known as "bifurcated fiber bundles" (BFBs), which is basically "*Y*" junction made of several glass fiber arranged in a bundle to increase the light collecting capability and extend the operating range [8]. Typically, to have a working range of few millimeters, bundles made with many fibers are required. This is specifically true for glass fibers; on the contrary, the same performance can be achieved with just a single plastic optical fiber, moreover, using very simple additional components such as an LED source and an amplified photodetector.

Many of such BFB configurations have already been investigated for the glass fiber case both from experimental and theoretical points of view [8, 9], but without considering the impact due to nonideal behavior of the fibers in the sensing head or of the target reflectivity.

The minimum sensor configuration to implement a target reflectivity compensation method requires the use of at least two fibers, namely, a transmitting (TX) and a receiving (RX) fiber, as sketched in Figure 1(a).

The target, at a distance d from the TX fiber surface, is lit by the transmitting circuit, and the reflected light is collected both by the transmitting fiber itself and by the receiving fiber and converted back to an electrical signal using receivers built on photodiodes and transimpedance amplifiers. A coupler is used to separate the forward and backward propagating signals in the transmitting fiber. Since the emitted beam spreads out of the transmitting fiber, the received power depends, among other parameters, on twice the fiber tip to target distance. The typical dependence of the signal received from the TX (ξ_{TX}) and RX (ξ_{RX}) fibers is shown in Figure 2 using normalized quantities.

The exact shape of the curves in Figure 2 depends on the fiber geometrical and optical parameters and on the alignment of their tips with respect to the target. However, it is clear that the power collected by the TX fiber exhibits a monotonic decrease with distance, while that of the RX fiber first increases, shows a maximum, and then decreases for larger distances.

Alternative, more complex, configurations can be implemented using more receiving fibers with longitudinal offsets to provide different signals, mainly used for compensation purposes [10].

2.2. Compensation of Target Reflectivity. Any compensation technique requires comparing at least two received signals with different dependence from the target distance. This can be obtained considering the signal received by the transmitting fiber and that from the receiving fiber or those from at least two receiving fibers with a longitudinal offset. The first choice is typically preferred because it leads to a more compact sensing head and to a higher sensitivity since the optical power collected by the TX fiber is higher than that of any RX fiber; however, it requires the use of a coupler
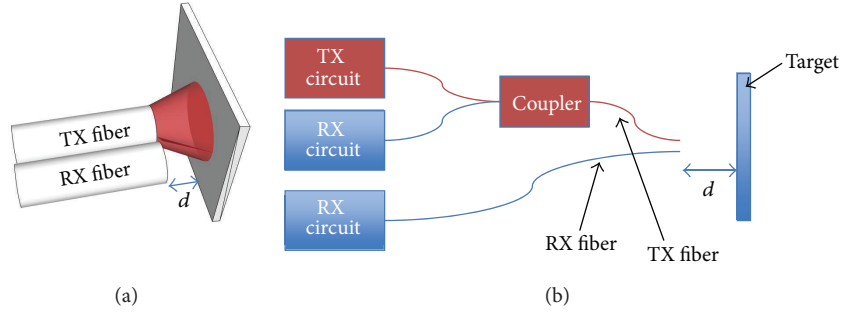
(a)

(b)

FIGURE 1: Schematic representation of the sensing head of a noncontact POF displacement sensor with one transmitting and one receiving fibers (a) and circuit connections to implement the proposed target reflectivity compensation technique (b).
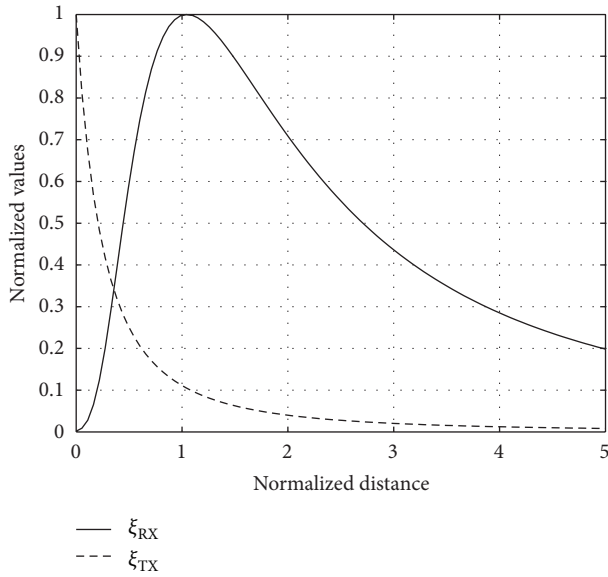

FIGURE 2: Typical theoretical behavior of the normalized expression for $\xi_{TX}(d)$ and $\xi_{RX}(d)$ versus the distance.

to separate incident and reflected signals in the transmitting fiber, and this introduces an additional source of errors due to its nonideal directivity. Actually, this contribution may be quite relevant since couplers for POF have quite a poor directivity due to the highly multimode working conditions.

Considering the approach with one TX and one RX fibers, in absence of noise, we can express the output voltage at the RX channel as

$$V_{RX}(d) = \eta_{RX} P_{in} R \xi_{RX}(d), \qquad (1)$$

where P_{in} is the input power, R is the target reflectivity, η_{RX} is an efficiency term that includes the optical attenuation within the fiber link, the responsivity of the photodiode, and the gain of the electrical amplifiers, and $\xi_{RX}(d)$ is the term that accounts for the dependence on the target distance. Analogously, for the TX fiber, we can write

$$V_{TX}(d) = \eta_{TX} P_{in} R \xi_{TX}(d) + V_{OFF}, \qquad (2)$$

where the distance dependence $\xi_{TX}(d)$ has a different profile with respect to that of RX fibers. For the TX fiber the output

voltage is no longer directly proportional to the reflectivity because of the offset V_{OFF}, which expresses the term due to the coupler directivity. Prior to defining the compensation technique, it is therefore necessary to remove this offset by subtracting the estimate of V_{OFF} from the V_{TX} term and obtaining an offset-compensated TX function $V_{TX,C}(d) = V_{TX}(d) - V_{OFF}$. Strictly speaking, V_{OFF} depends not only on the characteristics of the coupler, but also on the input power; however, once the system has been realized, an estimation can be easily obtained by placing the sensor far from the target or by terminating the TX fiber with an index matching medium.

The goal of the compensation strategy is to find a function of the output voltages that removes the double dependence on R and P_{in}. In the simplest form this can be obtained from the ratio of the signals from the TX and RX fibers V_{TX}/V_{RX}, as described in [7]. However, from experiments it has been verified that the efficiency of the reflectivity compensation procedure can be improved by using for the voltage-distance function the quantity S_C defined as

$$S_C(d) = \frac{V_{TX,C}(d)^M}{\left(V_{RX}(d) + \alpha V_{TX,C}(d)\right)^M}. \qquad (3)$$

Although such a choice from a theoretical point of view has no advantages over the simple TX/RX ratio, in practice setting $\alpha \neq 0$ avoids the denominator to approach a zero value, and choosing $M \neq 1$ allows reshaping the S_C slope, slightly tuning the sensitivity. From a set of experiments using standard 1 mm step index POF, the choice of $\alpha = 1$ and $M = 2.5$ has been made, so that S_C turned out to be a monotonic function in the range 0-1 with a roughly linear trend in the mid-point sensing range.

3. Theoretical Assessment of the Compensation Technique

3.1. The Numerical Method. An analytical description of the sensing system, as presented in [9], can be given only considering a simplified ideal case of fibers facing perpendicularly a target with uniform reflectivity and with a Gaussian irradiance. Such assumptions are excessively restrictive for the POF bundle.

Therefore, to consider more realistic cases, we used a Monte Carlo (MC) simulation technique, an approach that

Target position:
$z = (z' + d)$
$z'_a = z_a \cos(\alpha_x) \cos(\alpha_y)$

Hit target:
$x_t = (z'_a + d) \tan \theta_x$
$y_t = (z'_a + d) \tan \theta_y$

Fiber position
$(x_{RX3}, y_{RX3}, z_{RX3})$

Fiber hit condition:
$(x_h - x_{RX})^2 / a_x^2 + (y_h - y_{RX})^2 / a_y^2 < 1$

RX3

BW
$(0, 0, 0)$

Fiber facet plane:
$z = z_{RX2}$

y

TX

RX1

RX2

Interception:
$x_h = x_t + (z'_a + d - z_{RX2}) \tan \theta_x$
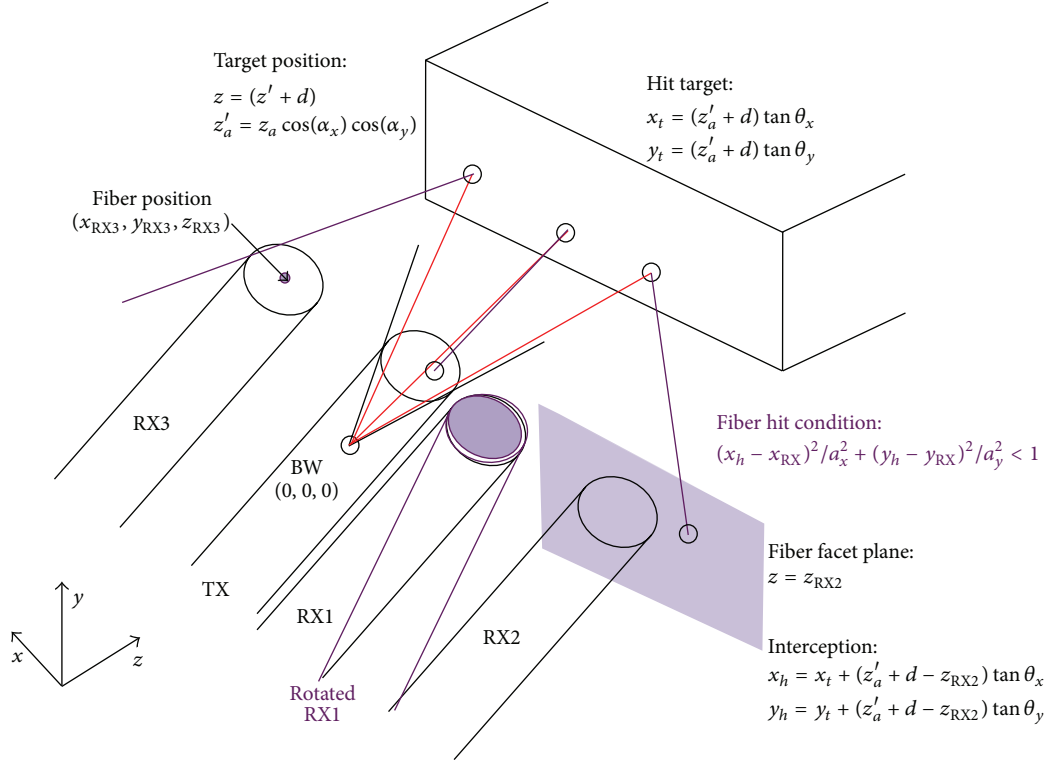$y_h = y_t + (z'_a + d - z_{RX2}) \tan \theta_y$

x

z

Rotated
RX1

FIGURE 3: Geometrical representation of the setup considered for the Monte Carlo simulations; to simplify, the target is considered as purely reflective.

is well known to provide an efficient way for the analysis of complex systems [11]. In optics this method is typically employed in the analysis of light propagation into scattering media [12], or in image ray-tracing algorithms [13]. MC approach owns few specific features: (1) it can simulate any type of irradiance; (2) it can take into account any rotation of the fibers and/or of the target; (3) it can implement both reflective and diffusive targets; (4) it can take into account targets with nonuniform reflectivity patterns.

The basic assumptions underlying MC fiber models are that the light emitted from the TX fiber can be represented as the superposition of a finite numbers M_1 of rays, each correspondent to a propagation direction, and that each ray carries a weight proportional to its power. Propagation along the air path, as well as reflection/diffraction of each ray is then treated analytically. Then, considering the catching surface of each fiber composing the bundle, we cumulate the number of backpropagated rays that hit each receiving fiber, each ray being weighted by its contribution to the optical power.

Figure 3 shows the geometry of the fiber bundle used for the MC simulation; to account for different positions of the receiving fiber while optimizing the simulation run times, a plurality of receiving fibers has been considered. All the fibers are assumed to have the same radius $r_F = 0.49$ mm and the same numeric aperture NA = 0.47, which corresponds to a critical angle $\varphi_C = \text{asin(NA)} = 28.03°$. Such values are typical nominal parameters of large core step index POF. The target is on the xy plane, and the z-axis is along the bundle-target

distance. The origin of the coordinate system is located in the beam waist (BW) of the TX fiber; the distance between the fiber end-surface and the BW is $z_a = r_F / \tan(\varphi_C) = 0.920$ mm. In order to consider TX fiber misalignments with respect to the xy plane, the angles α_x and α_y that describe the rotation of the TX fiber around x and y, respectively, are introduced; the TX fiber is rotated hinging on the BW, so that the projection of z_a on the z-axis is equal to $z'_a = z_a \cos(\alpha_x) \cos(\alpha_y)$.

Each MC sample corresponds to a ray composing the beam, which implies defining the angles θ_x and θ_y on the x-axis and y-axis, respectively. Angles are generated independently as random variables with uniform distribution; then, a suitable rejection technique sets the desired joint probability density function (PDF) $f(\theta_x, \theta_y)$ in order to best approximate the light emitted from the core of the TX fiber, considering also the rotations α_x and α_y. In other words, each randomly generated pair (θ_x, θ_y) is accepted with probability $p(\theta_x, \theta_y)$ and rejected otherwise. For instance, for a uniform irradiance in a cone defined by the NA the acceptance probability is 1 if $(\theta_x - \alpha_x)^2 + (\theta_y - \alpha_y)^2 < \varphi_C^2$ and 0 otherwise. A better approximation of POF emission beam is in terms of a two-dimensional super Gaussian profile; this implies that the pair (θ_x, θ_y) is accepted with probability p equal to

$$p(\theta_x, \theta_y) = \exp\left\{ -\frac{1}{2\sigma^2} \left[(\theta_x - \alpha_x)^2 + (\theta_y - \alpha_y)^2 \right]^{2G} \right\}, \quad (4)$$
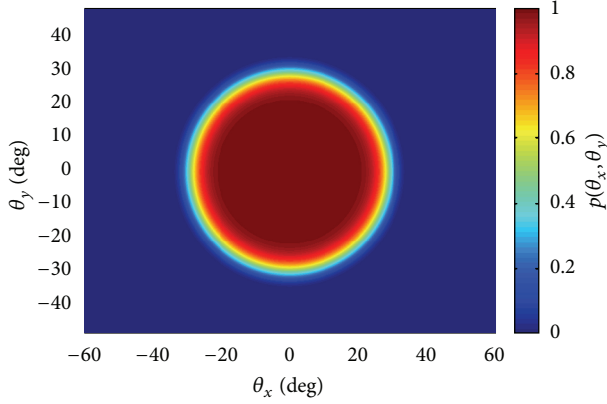
FIGURE 4: Ray acceptance probability for a super Gaussian emission matching the field profile of a standard step-index POF. Parameters: $G = 3$, $\varphi_C = 28.03°$, $\sigma = \varphi_C^{2G}$, and $\alpha_x = \alpha_y = 0°$.
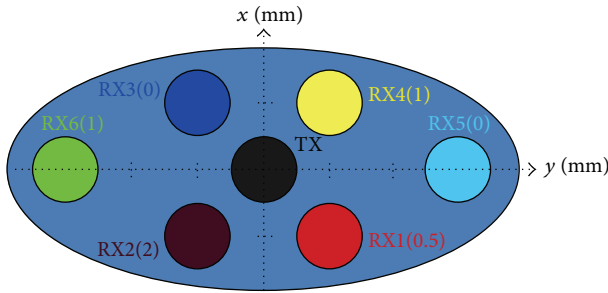

FIGURE 5: Sample fiber bundle for MC analysis. RX1–RX4 fibers are centered in $x, y = \pm 1$ mm and retracted by 0.5 mm, 2 mm, 0 mm, and 1 mm on the z-axis, respectively; RX5-RX6 are centered at $x = 0$ mm and $y = \pm 3$ mm and retracted by 0 mm and 1 mm.

where σ is the standard deviation and G is the super Gaussian order. By setting $G = 3$ and $\sigma = \varphi_C^{2G}$ (φ_C in radians), a good reproduction of the output beam of plastic fiber as measured in standard step index POF is obtained [14]. Figure 4 reproduces the acceptance probability p as a function of θ_x and θ_y for this approximation, assuming that $\alpha_x = \alpha_y = 0°$. This expression of the light irradiance has a quasiflat profile in the central part and rapidly decreases close to the NA edge, as typical for POF.

Each ray starting from the point $(0, 0, 0)$ hits the target in the position $(x_t, y_t, z'_a + d)$, where $x_t = (z'_a + d) \tan \theta_x$ and $x_y = (z'_a + d) \tan \theta_y$. As the ray hits the target, ideally it should be backpropagated according to bidimensional Snell's law; however, in order to have a more realistic modelling of the target surface, diffusiveness from target surface can be further taken into account through a second-order Monte Carlo. In this case, each of the M_1 propagated rays is split into one reflected ray that accounts for pure Snell reflection and M_2 rays, each one with pair of angles (ϕ_x, ϕ_y) that describe the extra rotation of the diffused ray with respect to Snell ray. Again, the (ϕ_x, ϕ_y) pairs are generated from a set of uniformly

distributed angles, applying a rejection technique as in (4) as follows:

$$p\left(\phi_x, \phi_y\right) = \exp\left[-\frac{1}{2\sigma_D^2}\left(\phi_x^2 + \phi_y^2\right)^{2H}\right], \quad (5)$$

where the diffusion from target is modeled with a super Gaussian pattern. All the diffused rays have equal weight D/M_2, while the Snell ray has weight $(1-D)$, so that the sum of the two contribution is unitary and the total diffusion power component is D. The target has a punctual reflectivity equal to $R(x,y)$; hence, the weight of each ray is multiplied by the reflectivity on the impact point $R(x_t, y_t)$. With comparison to the other more complex theoretical modeling of diffusive surfaces, the adoption of a super Gaussian pattern allows an easier computation as it encodes in only three straightforward parameters (D, H, and σ_D) for the type of surface, while preserving a good match between simulated and experimental diffusion patterns; for a more accurate modeling, it is possible to replace the Metropolis rejection equation (5) with a different probability density function.

The receiving bundle is composed by NRX fibers and one TX fiber. Each RX fiber can be rotated by β_{xi} and β_{yi}, $i = 1, \ldots, N$, and its end-surface is centered in the point $(x_{\mathrm{RX}i}, y_{\mathrm{RX}i}, z_{\mathrm{RX}i})$, as depicted in Figure 3. The received signal from the TX fiber is treated as those of the other RX fibers. The ray catching area of each fiber has elliptic section with semiaxes $a_{xi} = r_F \cos(\beta_{xi})$ and $a_{yi} = r_F \cos(\beta_{yi})$, obtained as the projection of the fiber surface on the xy plane with respect to fiber misalignments β_{xi} and β_{yi}. With these assumptions, the ray arrival position, that is, the xy coordinates on the fiber facet plane $z = z_{\mathrm{RX}i}$ after the forward and backward paths, is calculated as

$$x_{hi} = \left(z'_a + d\right) \tan\left(\theta_x\right) + \left(z'_a + d - z_{\mathrm{RX}i}\right) \tan\left(\theta_x + \phi_x\right),$$

$$y_{hi} = \left(z'_a + d\right) \tan\left(\theta_y\right) + \left(z'_a + d - z_{\mathrm{RX}i}\right) \tan\left(\theta_y + \phi_y\right). \quad (6)$$

Hence, the hit condition is that the arrival point (x_{hi}, y_{hi}) falls inside the ellipse centered in $(x_{\mathrm{RX}i}, y_{\mathrm{RX}i})$ and having a_{xi} and a_{yi} as semiaxes as follows:

$$\frac{\left(x_{hi} - x_{\mathrm{RX}i}\right)^2}{a_x^2} + \frac{\left(y_{hi} - y_{\mathrm{RX}i}\right)^2}{a_y^2} < 1. \quad (7)$$

This approximation of the collecting area is valid only for low misalignments (as it should be the typical sensor working condition), since it neglects the guidance of the received photons into the receiving fibers.

Thus, by evaluating which of the $M_1(1 + M_2)$ rays hit each fiber catching area and cumulating their weights, a quantity proportional to the received optical power in each POF composing the bundle is determined, obtaining thus an estimation of the $\xi_{\mathrm{TX}}(d)$ and $\xi_{\mathrm{RX}}(d)$ functions.

3.2. Performance Analysis. The MC simulation is an effective tool for design, simulation, and performance analysis of the POF bundle. In this section, it is applied to a sample fiber
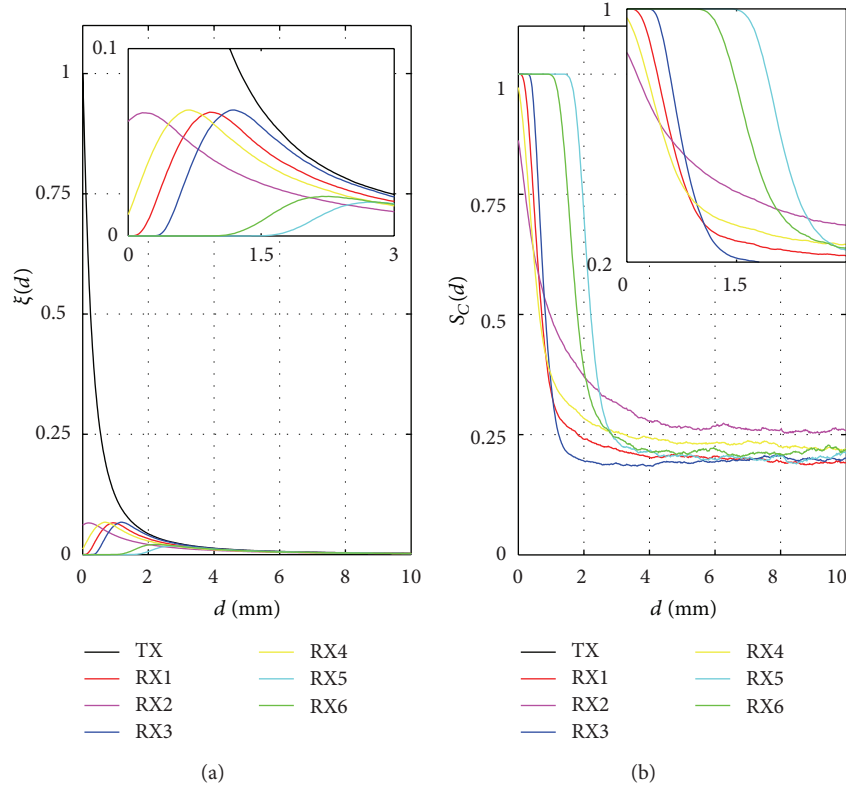
(a)

(b)

FIGURE 6: (a) $\xi_{TX}(d)$ and $\xi_{RX}(d)$ functions for each TX/RX fiber of the sample bundle. (b) $S_C(d)$ functions for each RX fiber. Insets zoom on the close-range portion of the charts.
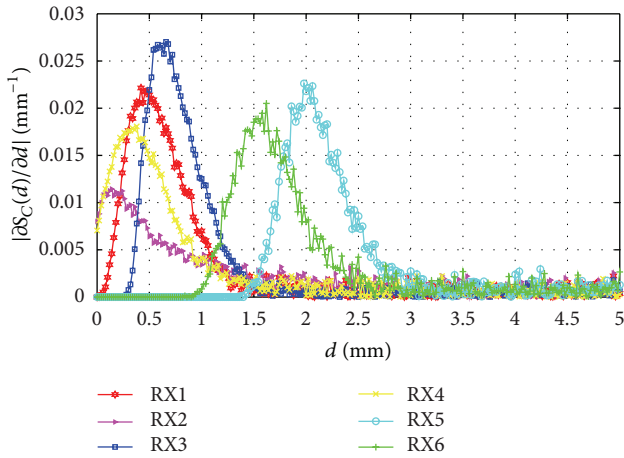

FIGURE 7: Derivative of the compensation functions for the sample fiber bundle.

bundle composed of 6 RX fibers (Figure 5) to simultaneously consider with a single run different combinations of positions in the xy plane and offsets with respect to the transmitting fiber tip. In particular, RX1 to RX4 fibers are centered in $(x, y) = \pm 1$ mm and retracted by 0.5 mm, 2 mm, 0 mm, and 1 mm on the z-axis, respectively, while RX5 and RX6 are centered at $x = 0$ mm and $y = \pm 3$ mm and retracted by 0 mm and 1 mm.

Figure 6(a) plots the ξ_{TX} and ξ_{RX} curves as a function of target displacement d for a reflective target with no rotation and uniform reflectivity. As expected, the TX curve has a monotonic trend, while each RX curve has a peak centered at a distance that depends on the considered receiving fiber position with respect to the transmitting one. The chart shows that the peak of ξ_{RX} moves to shorter distances when the RX fiber has a longitudinal offset from the TX fiber plane, or when the fiber is moved away from the TX fiber. In the latter case, the maximum received power is also lower. All curves tend to converge for long distance. Figure 6(b) plots the compensated functions S_C evaluated as in (3) for each RX fiber; this function has a steep monotonic descent for a displacement range of ~1.3 mm for each fiber, which represents the useful region of the simulated sensor; the maximum sensitivity point is reached nearly halfway along the useful range. Changing the fiber position the useful range can be tuned for different ranges of displacement, as clearly shown for fibers RX5-RX6 for which the useful range is shifted to $d > 2$ mm. However, it should be considered that there is always a tradeoff between the shift of the peak position and the received power so that, in practice, the shift cannot be larger than few millimeters.

This concept is further emphasized in Figure 7, which reports the derivative of the compensation function $|\partial S_C/\partial d|$. This function shows that each RX fiber has a sensitivity peak in a region that extends for about 1 mm around a specific displacement that depends on the fiber position. This
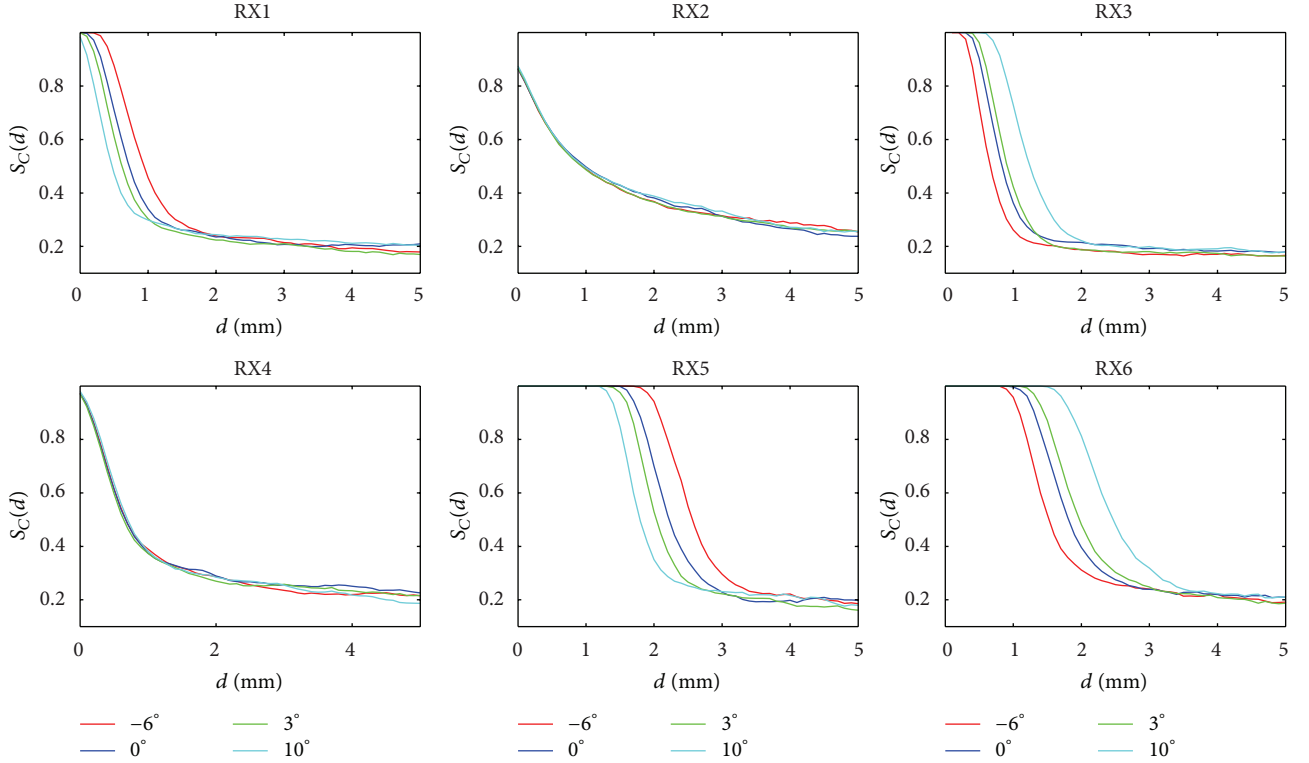
FIGURE 8: $S_C(d)$ functions for each RX fiber for a horizontal target rotation of $-6°$, $0°$, $3°$, and $10°$. RX2 and RX4 fibers, the most retracted from TX along z-axis, appear to be rotation insensitive, as they are more shadowed.

also suggests that, by using multiple fibers with different positioning, the optimum working range can be extended by proper selection of the receiving fiber.

Occasionally, due to fabrication tolerances or errors in the sensor use, the target could be rotated by a certain small angle. To account for this case, Figure 8 reports the plot of the S_C curve for each RX fiber for different values of target rotation along the horizontal axis; as expected, the target rotation induces a left or right shift of the working range and, hence, changes the displacement readout. Table 1 reports a quantitative evaluation of the errors induced by a target rotation, and, given the large differences among the receiving fibers, it can be concluded that the tolerance to fiber rotation is strongly dependent on the bundle design.

The MC simulation can be also used to study the effect of a nonuniform target reflectivity. In principle the fiber bundle system can compensate for any reflectivity variation, due, for example, to day/night or light/shadow transitions, surface yellowing through aging, or dust. However, if such a variation is not uniform on the target surface, it might lead to a nonideal compensation that affects the system performance. In order to evaluate the incidence of this nonideal behavior, a set of simulations considering a spot with radius 2 mm with different reflectivity on the target placed in front of the TX fiber or 1 mm aside have been considered. Empirically, this is an almost worst-case scenario as the reflectivity variation is abrupt, close to irradiance point, and intercepts a wide amount of the transmitted light. Figure 9 shows that the compensation technique is fairly tolerant to reflectivity

variations; all S_C curves are almost superimposing, even for a worst-case unrealistic scenario of a steep 45% reflectivity variation.

Finally, the different behavior of reflective and diffusive target surfaces has been simulated with the MC method. In general, the more diffusive the target is (i.e., higher values of D and ϕ_x, ϕ_y in (5)), the lower the peak value of the received power is, and the higher the value of power collected toward the long displacement side of the curve will be. Figure 10 reports the $S_C(d)$ functions for different cases, in which $\phi_x = \phi_y = \phi_d$. RX5 and RX6 fibers, which are those placed far from TX fiber, exhibit a stronger dependence on D and ϕ_d.

To summarize, the MC simulation provides qualitative and, with some approximations, quantitative information on the POF bundle compensated sensor; sensitivity, tolerance, and quality of compensation have a fairly strong dependence on fiber positioning in the bundle.

4. Experimental Results and Discussions

The scheme in Figure 1 has been implemented using commercial step index fibers, having 980 μm PMMA core made surrounded by a perfluorinated 10 μm layer acting as the cladding; the numerical aperture is close to 0.5. Both TX and RX fibers are covered with a black jacket in order to reduce the cross-talk when in close proximity. The setup then includes a current driven 650 nm LED source and a home-made two-channel receiver having one input connected to the transmitting fiber through a commercial 3 dB coupler and the
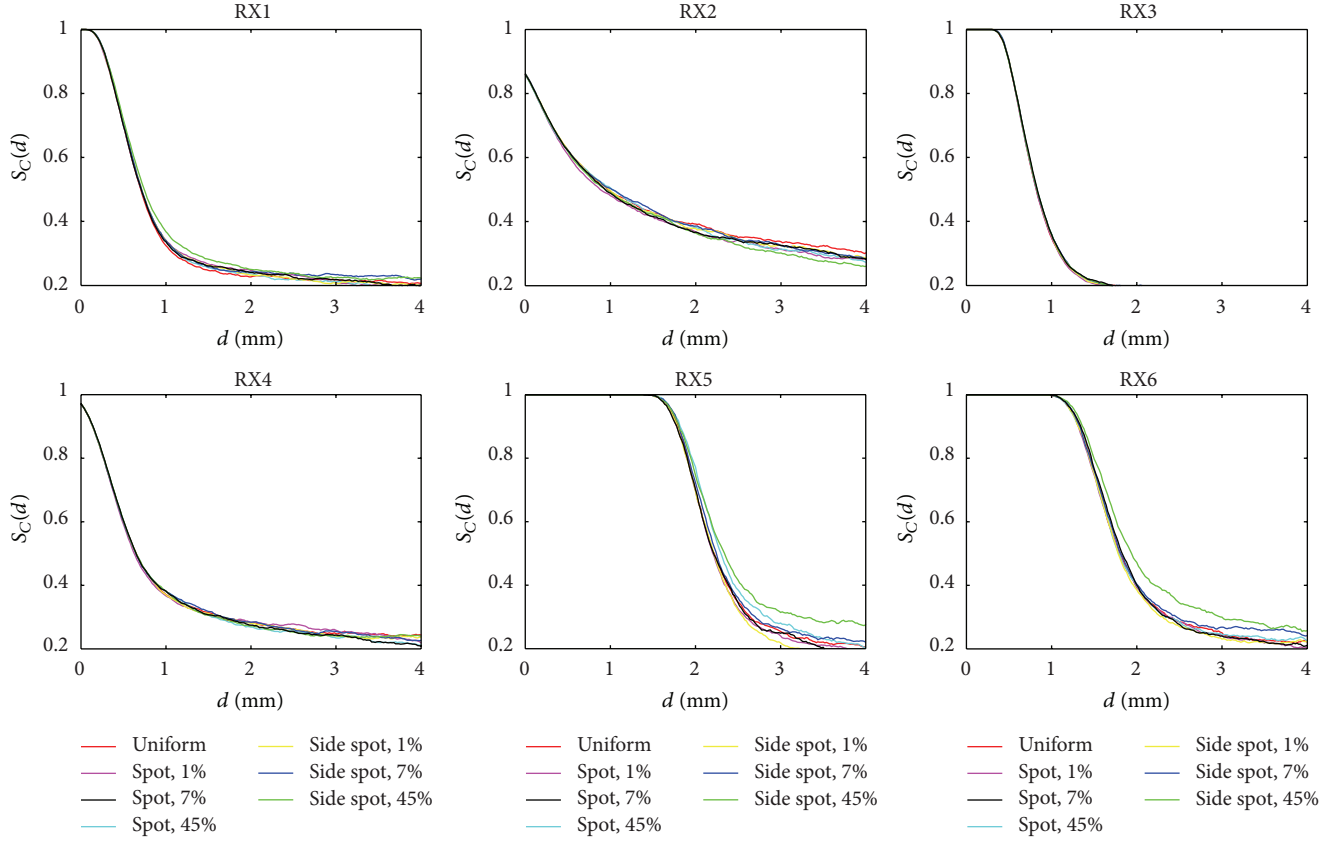
FIGURE 9: $S_C(d)$ functions for all RX fibers in presence of a spatially nonuniform target reflectivity; the chart reports result for a circular spot with radius 2 mm and with reflectivity variation of 1%, 7%, and 45% from the target nominal reflectivity, either facing the TX fiber (spot) or centered 1 mm aside along x-axis (side spot).

TABLE 1: Displacement readout variation for each degree of target horizontal rotation—reported for each RX fiber for 3 different S_C values representing near, mid, and far working range.

S_C	RX1	RX2	RX3	RX4	RX5	RX6
$S_C = 0.35$	$-32.1\,\mu m/°$	OR	$+41.3\,\mu m/°$	$+6.5\,\mu m/°$	$-51.4\,\mu m/°$	$+62.4\,\mu m/°$
$S_C = 0.60$	$-27.3\,\mu m/°$	$+2.8\,\mu m/°$	$+34.0\,\mu m/°$	$+4.4\,\mu m/°$	$-46.8\,\mu m/°$	$+56.0\,\mu m/°$
$S_C = 0.95$	$-21.6\,\mu m/°$	OR	$+25.7\,\mu m/°$	$+4.9\,\mu m/°$	$-38.0\,\mu m/°$	$+44.8\,\mu m/°$

OR: out of working range.

other to the receiving only fiber. The gains of the two channels have been adjusted to have output signals of approximately similar order of magnitude; then, these signals are imported in program developed in LabView through a commercial 16-bit DAQ card with maximum sampling capability of 250 kS/s. The LED is modulated at about 1 kHz so that it is possible to use a synchronous acquisition scheme to suppress stray light and environmental noise.

The sensing head has then been mounted on a precision computer controlled linear translation stage and used to measure the distance from a set of targets with different reflectivity and surface patterns. These targets include paper sheets with a quite rough surface and with five different colors, to simulate a diffusive target with variable reflectivity; a layer of tin foil, to provide a highly reflective surface with a nonideal facet; a bar of opaque steel, to represent a typical industrial application of the POF sensor; a mirror, to

simulate a purely reflective object with maximum reflectivity (in practical applications, a mirror surface can also be applied in front of a poorly reflective target like, e.g., black plaster). Compensation of target reflectivity is performed as in (3), by setting $\alpha = 1$ and $M = 2.5$.

Having the goal of optimizing the performance for close range applications, the experiments have been mainly conducted using a configuration with the RX fiber center positioned at about 1.2 mm from the TX fiber and without longitudinal offset.

Figure 11 depicts the output voltages at the receiver for this configuration as a function of the target displacement for several target types. The profile of these functions well reproduces the theoretical behavior of Figure 2, as well as the simulated behavior in Figure 6; TX signals are monotonically decreasing with displacement, while RX ones have a peak around $d = 0.95$ mm. The $V_{TX,C}$ and V_{RX} profiles for the
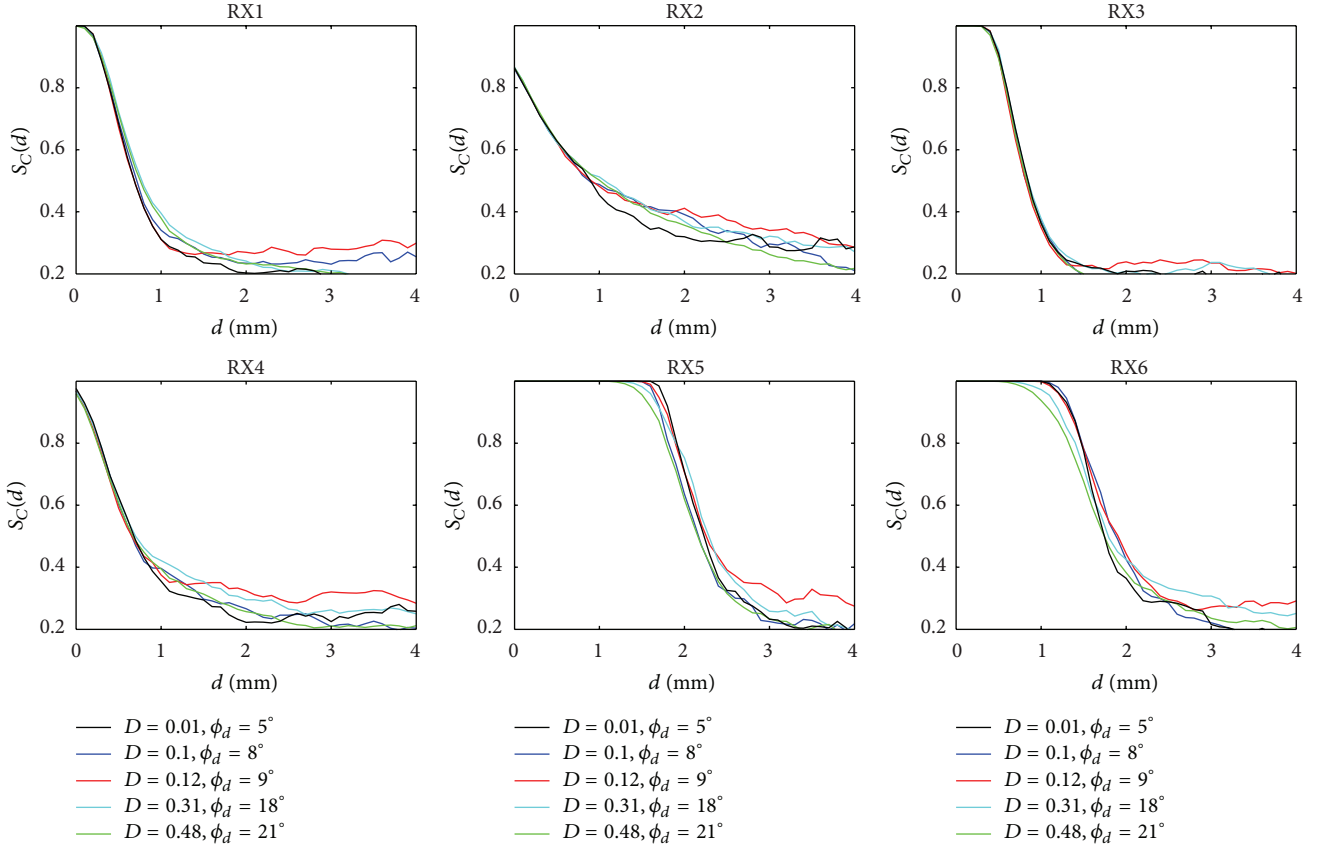
FIGURE 10: $S_C(d)$ functions for the sample bundle for different diffusivity profiles of the target surfaces; D and $\phi_d = \phi_x = \phi_y$ are defined in Section 3.1.

colored paper targets (with the following nominal reflectivity values: 25% for the blue, 30% for the green, 40% for the yellow, 45% for the white, and 50% for the pink) follow the same pattern, and the curves are almost proportional each other. The opaque steel has about 40% reflectivity and the correspondent RX curve has a steeper increase in the initial $d = (0\text{-}1)$ mm range with respect to paper targets—actually, it hits the maximum voltage point in correspondence of white paper, which is 45% reflective—and a steeper decrease for long displacements; this result is compatible with surface analysis of Figure 10. The tin foil and mirror targets are highly reflective, but their surface is significantly different; the RX curve for the mirror surface appears to be the steepest one, while there is a slight misalignment of 0.5 mm of the peak position for the tin foil curve, possibly attributable to its irregular surface.

Figure 12 reports the $S_C(d)$ functions for all these different types of targets. The chart shows a good superposition of the S_C functions for all the target typologies, particularly in the close range (0-1) mm. As a matter of fact, the comparison of paper targets, which ideally should have exactly the same pattern, shows indeed a remarkable superposition of the curves. On the other hand, reflective targets have a slightly different profile, with opaque steel and tin foil almost superposed and mirror having a slightly higher S_C. Considering both cases, the maximum useful range for the

specific configuration is limited by noise and is of about 2 mm. Unlike the curves reproduced in Section 3.2, the $S_C(d)$ reaches a value smaller than that obtained through simulations; this is due to a different gain of the electrical amplifiers, which results in $\eta_{TX} \neq \eta_{RX}$ while MC simulation does not consider the electrical amplification factor. However, a good match on the useful range is provided. The key asset of this type of sensing system, that is, the compensation of target reflectivity that is imperative for most prominent industrial applications, is hereby demonstrated.

The working range determination is also supported by the evaluation of the sensitivity with displacement (Figure 13); the peak is at about $d = 0.17$ mm and usable values are up to 1.6 mm, although in order to work in the higher sensitivity region, this configuration is recommended for the conservative range (0-1) mm.

Figure 14 reports the comparison between the $S_C(d)$ functions, evaluated for paper targets, and the MC simulation for the same fiber bundle. The chart highlights an almost perfect superposition of the functions on the (0–1.2) mm displacement range, with the curves having the same behavior. The MC-simulated curves tend to diverge from the experimental functions for $d > 1.2$ mm, which is, however, out of the working range of the sensor; in this region, although both simulated and experimental curves have a similar behavior, they reach a different plateau.
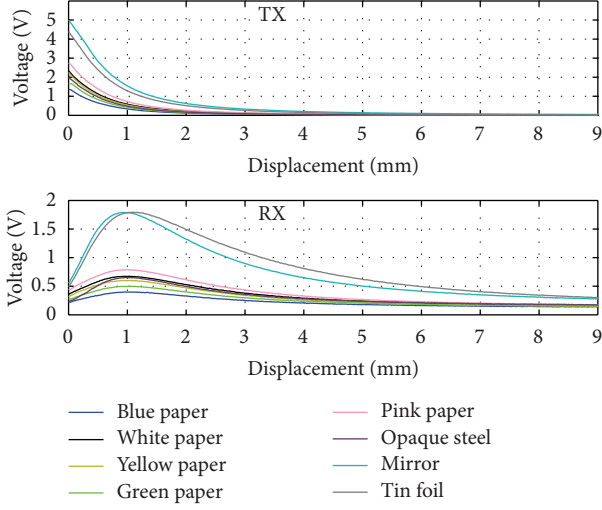
FIGURE 11: Experimental $V_{TX,C}$ and V_{RX} curves as a function of target displacement, for 8 different target profiles. An offset V_{OFF} = 1.91 V has been subtracted from all TX voltages to compensate for directivity of the POF coupler.
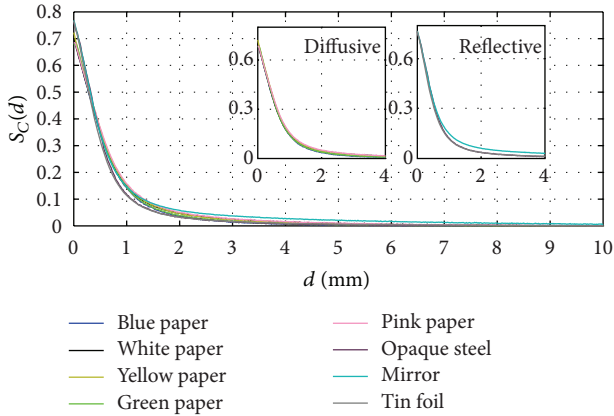

FIGURE 12: Evaluation of the $S_C(d)$ curves for the different targets. Left inset zooms on the close-range portion for diffusive paper targets, and right inset zooms on more reflective targets (steel, mirror, and tin foil).

Finally, in order to provide a more quantitative estimation of the performances of the sensor and in particular the effectiveness of the reflectivity compensation, Figure 15 and Table 2 report the difference between the displacement measured with each colored paper target and the displacement imposed by a computer controlled micropositioner (taken as the reference value). The underlying assumption is that the $S_C(d)$ curves of the paper target should perfectly overlap since all these targets have the same surface pattern but different color. However, in practice this measure includes also the effect of target misalignments because in the used setup changing the color of the target implies mounting and unmounting of the target. Considering the results in Figure 14, a good overlap of the curves, particularly in the (0–0.8) mm range, demonstrates the effectiveness of the
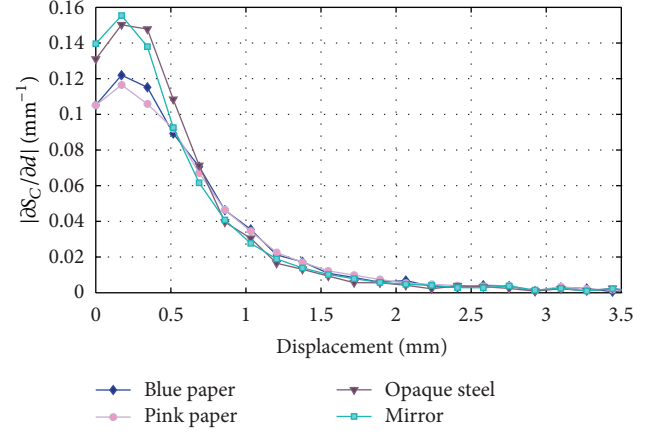

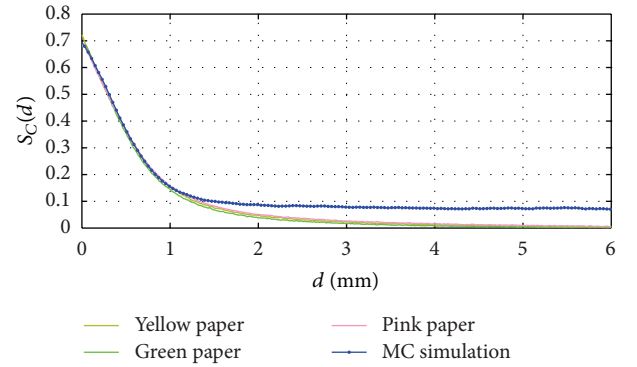FIGURE 13: Sensitivity of the $S_C(d)$ curves with displacement.

FIGURE 14: Comparison of $S_C(d)$ curves for paper targets and correspondent MC simulation.

TABLE 2: Summary of compensation performances of the proposed sensor.

Target	Reflectivity	Max $|d_{meas} - d_{ref}|$
Blue paper	25%	33 μm
Green paper	30%	20 μm
Yellow paper	40%	13 μm
White paper	45%	17 μm
Pink paper	50%	23 μm

proposed compensation approach, with a maximum error of 33 μm. Then, for longer displacements, the lack of sensitivity deteriorates the overlapping, with readout difference over 0.1 mm.

5. Conclusion

A low-cost fiber-based sensor for noncontact short-range displacement measurements has been presented and its performance evaluated. The sensor is made by two plastic optical fibers, and the displacement is calculated from the variation in the power received after reflection from the target whose displacement has to be evaluated, compensating for
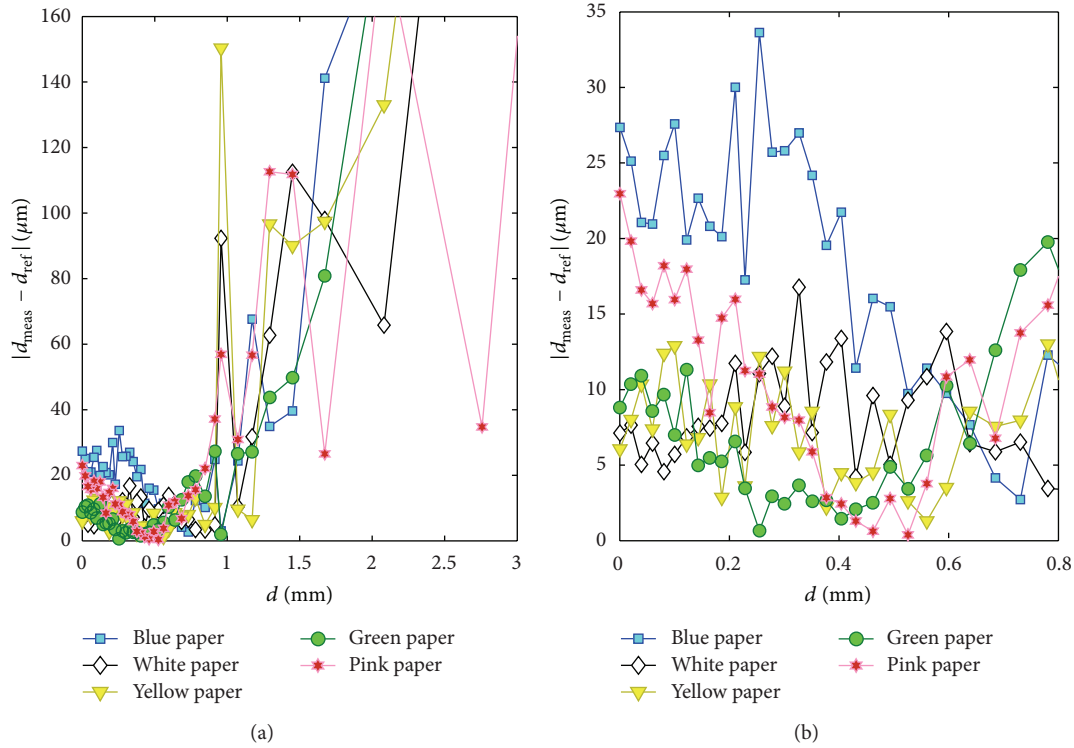
FIGURE 15: Difference between displacement readout d_{meas} and the reference displacement d_{ref}, for colored paper targets (a) and detail for the short-range region (b).

target reflectivity changes. A model of the sensor has been developed, and the impacts of sensing head design choices on the performances have been studied first through a Monte Carlo simulation approach, and then experimental tests have been carried out on a sensor designed to operate in the (0-1) mm range. The results have demonstrated the effectiveness of the proposed configuration, which has allowed keeping the error below 0.04 mm in a broad reflectivity range.

References

[1] K. Peters, "Polymer optical fiber sensors—a review," *Smart Materials and Structures*, vol. 20, no. 1, Article ID 013002, 2011.

[2] M. Olivero, G. Perrone, A. Vallan, and S. Abrate, "Plastic optical fiber displacement sensor for cracks monitoring," *Key Engineering Materials*, vol. 347, pp. 487–492, 2007.

[3] G. Perrone and A. Vallan, "A low-cost optical sensor for noncontact vibration measurements," *IEEE Transactions on Instrumentation and Measurement*, vol. 58, no. 5, pp. 1650–1656, 2009.

[4] A. Vallan, M. L. Casalicchio, and G. Perrone, "Displacement and acceleration measurements in vibration tests using a fiber optic sensor," *IEEE Transactions on Instrumentation and Measurement*, vol. 59, no. 5, pp. 1389–1396, 2010.

[5] S. Donati, *Electro-Optical Instrumentation: Sensing and Measuring With Lasers*, Prentice Hall, Upper Saddle River, NJ, USA, 2004.

[6] P. M. B. Silva Girào, O. A. Postolache, J. A. Brandào Faria, and J. M. C. Dias Pereira, "An overview and a contribution to the optical measurement of linear displacement," *IEEE Sensors Journal*, vol. 1, no. 4, pp. 322–331, 2001.

[7] M. L. Casalicchio, A. Neri, G. Perrone, D. Tosi, and A. Vallan, "Non-contact low-cost fiber distance sensor with compensation of target reflectivity," in *Proceedings of the IEEE Intrumentation and Measurement Technology Conference (I2MTC '09)*, pp. 1671–1675, May 2009.

[8] J. A. Gilbert, M. E. Schultz, and A. J. Boehnlein, "Remote displacement analysis using multimode fiber-optic bundles—multimode fiber-optic bundles are used to holographically measure displacement," *Experimental Mechanics*, vol. 22, no. 10, pp. 398–400, 1982.

[9] J. B. Faria, "A theoretical analysis of the bifurcated fiber bundle displacement sensor," *IEEE Transactions on Instrumentation and Measurement*, vol. 47, no. 3, pp. 742–747, 1998.

[10] X. Li, K. Nakamura, and S. Ueha, "Reflectivity and illuminating power compensation for optical fibre vibrometer," *Measurement Science and Technology*, vol. 15, pp. 1773–1778, 2004.

[11] M. H. Kalos and P. A. Whitlock, *Monte Carlo Methods*, John Wiley & Sons, 1986.

[12] J. C. Ramella-Roman, S. A. Prahl, and S. L. Jacques, "Three Monte Carlo programs of polarized light transport into scattering media: part I," *Optics Express*, vol. 13, no. 12, pp. 4420–4438, 2005.

[13] H. W. Jensen, J. Arvo, M. Fajardo et al., "State of the art in Monte Carlo ray tracing for realistic image synthesis," in *Proceedings of the Association for Computing Machinery's Special Interest Group on Computer Graphics and Interactive Techniques (SIGGRAPH '01)*, 2001.

[14] A. Vallan, M. L. Casalicchio, M. Olivero, and G. Perrone, "Two-dimensional displacement sensor based on plastic optical

fibers," *IEEE Transactions on Instrumentation and Measurement*, vol. 62, no. 5, pp. 1233–1240, 2013.